Theoretical calculation guided design of single atom-alloyed bismuth catalysts for ampere-level CO_2 electrolysis to formate

Haidong Shen [1], Tianshuai Wang [*,1], Hao Jiang, Peng Zhao, Zhanwei Chen, Yingzhe Feng, Yueling Cao, Ying Guo, Qiuyu Zhang [*], Hepeng Zhang [*]

Xi'an Key Laboratory of Functional Organic Porous Materials, School of Chemistry and Chemical Engineering, Northwestern Polytechnical University, Xi'an 710129, PR China

ARTICLE INFO

ABSTRACT

Electrochemically reducing CO_2 (CO_2RR) to value-added fuels is a promising strategy to achieve carbon neutralization. Nowadays Bi-based catalysts suffer from limited activity, selectivity, and stability under harsh condition. Herein, under the guidance of density functional theory calculations, Zn single-atom alloyed metallic Bi (SAA-Zn_1Bi) was screened out as the remarkable CO_2RR catalyst for formate production. As expected, SAA-Zn_1Bi, synthesized by a two-step in-situ electrochemical reduction strategy, delivered an industrial-compatible current density of -1323 mA cm^{-2} and exhibited a record formate formation rate of 24.5 mmol·h^{-1}·cm^{-2} at -0.86 V versus the reversible hydrogen electrode. Importantly, the durability reaches 250 h at -400 mA cm^{-2} was realized. The in-situ experimental explorations revealed that SAA-Zn_1Bi benefited from its moderately adsorbed *OCHO intermediate, matched well with the precast of the theoretical calculations. This work is highly instructive for the design of SAAs electrocatalysts and provides a new avenue for the fabrication of Bi-based SAAs electrocatalysts.

1. Introduction

The electrocatalytic conversion of CO_2 into liquid fuels using renewable resources is an emerging and promising pathway to diminish the greenhouse effect and energy crisis [1–3]. Among various reduction possibilities, formate (C1 product, generated via a two-electron process) is one of the most economical chemicals [4] owing to its high volumetric energy density and expedient integration with existing infrastructure [5,6]. Among numerous formate-selective electrocatalysts (Pb [7], Sn [8], In [9], Bi [10] and Cd [11] et al.), Bismuth-based (Bi-based) materials exhibit tremendous attraction due to environmentally friendly, earth abundance and low cost. Recently, many up-and-coming strategies, including defect engineering [12,13], interface engineering [14,15], morphology modifications [16,17], strain modulation [18,19] and heteroatom doping [20,21], have been devoted to modulating the electronic and microcosmic structure of Bi-based electrocatalysts, then adjusting their binding energy with adsorbates [22], thereby improving the activity of Bi-based electrocatalysts. Despite such inspiring results, achieving the industrial requirements with long-term stability for

Bi-based electrocatalysts under a high current density condition remains a critical hurdle [15,17], and breakthroughs remain needed in catalyst design.

Recently, an essential development in this field is employing single-atom alloys (SAAs) engineering to ameliorate the electrocatalytic performance under harsh industrial conditions. Unlike traditional doping strategies, SAAs possess the features of maximum utilization of the metal atoms [23], uniform active sites [24,25], and peculiar geometric and electronic structures [26,27], which endows them with excellent catalytic behavior for electrocatalytic reduction of CO_2 [7,28,29]. For example, Zeng's group [7] reported a single-atom Pb-alloyed Cu catalyst (Pb_1Cu) that can exclusively (~96% Faradaic efficiency (FE)) convert CO_2 into formate with high activity over 1 A cm^{-2}. However, the studies about Bi-based SAAs for CO_2RR remain undeveloped to date. Considering the exceptional properties of SAAs, it inspires us to check if the concept of SAAs engineering can be used to guide the design of Bi-based materials for improving the activity of formate production under harsh industrial conditions. Nevertheless, it will be time-consuming and labor-intensive to find out an efficient foreign metal for constructing

effective Bi-based CO_2RR SAAs electrocatalysts due to the multitudinous metals. Compared with the traditional experimental exploration process, theoretical calculation exhibits tremendous attraction for screening catalysts with excellent performance as a result of its efficient, economical, and accurate features, which has achieved great success in recent studies [30,31].

Herein, density functional theory (DFT) calculations were employed to build up a full picture of the potential of nine Bi-based single-atom alloys (denoted as SAA-X_1Bi, X = Sc, Ti, V, Mn, Fe, Co, Ni, Cu, and Zn) catalysts for the electrocatalytic CO_2-to-formate conversion. Combination with the grey correlation analysis, we revealed that the *OCHO adsorption strength was the crucial factor in influencing the overpotential of SAA-X_1Bi for electrocatalyzing CO_2 to formate, and SAA-Zn_1Bi exhibited the best electrocatalytic properties due to the moderate adsorption strength towards *OCHO. According to the adsorption capacity to *OCHO obtained by the calculations, three typical catalysts, SAA-Zn_1Bi (moderate adsorption), SAA-Mn_1Bi (strong adsorption), and pristine Bi (weak adsorption) were synthesized by a concise in-situ transformation strategy. The electrocatalysis results demonstrated the most dramatic activity enhancement for SAA-Zn_1Bi in electrocatalytic CO_2-to-formate conversion (an industrial-compatible current density of -1323 mA cm^{-2}, a record formate formation rate of 24.5 mmol·h^{-1}·cm^{-2} at -0.86 V versus the reversible hydrogen electrode (V_{RHE}), a wide operation window (1100 mV, from -0.35 to -1.45 V_{RHE}) for the formate FE of > 90%, and long-term stability for more than 250 h at a current density of -400 mA cm^{-2}), which matched well with the conclusions of the DFT calculations.

2. Experimental section

2.1. Chemical reagents

Bismuth nitrate ($Bi(NO_3)_3 \cdot 5$ H_2O, 99.8%), zinc nitrate ($Zn(NO_3)_2 \cdot 6$ H_2O, 99.8%), manganese nitrate ($Mn(NO_3)_2 \cdot 6$ H_2O, 99.8%) and KOH (99.8%) were purchased from Sinopharm Chemical Reagent Co., Ltd. Dimethyl sulfoxide (DMSO, 99.5%), ethanol (99.7%), L-cysteine (99.8%), ethanolamine (99%) were purchased from Guangdong Guanghua Sci-Tech Co., Ltd. The above reagents were of analytical grade and used directly without any further purification before the experiment. The gas diffusion layer (GDL) (Sigracet 29 BC) and the anion exchange membrane (Nafion 115) was purchased from Fuel Cell Store. Nafion solution (5 wt%) was purchased from Sigma-Aldrich LLC. The gas used in experiments: high-purity Argon (Ar, > 99.999%), high-purity carbon dioxide (CO_2, > 99.999%). The ultrapure water (>18.25 MΩ cm) was used for the experiments.

2.2. Materials synthesis

2.2.1. Synthesis of M-Bi_2S_3 (M=Mn and Zn) nanosheet precursor

The Zn-Bi_2S_3 nanosheet precursor was synthesized via a modified hydrothermal method. Typically, 0.97 g of $Bi(NO_3)_3 \cdot 5$ H_2O, a certain amount of $M(NO_3)_2 \cdot 6$ H_2O (M=Mn and Zn; the atom ratio of M/Bi is 0.05), and 0.484 g of L-cysteine were dispersed in 54 mL of ultrapure water and stirred for 30 min with a rotation speed of 450 r/min. Then, 6 mL of ethanolamine was added, and the mixture was stirred for another 30 min. After that, the resulting solution was transferred into a 100 mL Teflon-lined stainless-steel autoclave and heated at 160 °C for 3 h. Finally, the solid was collected by centrifugation and then washed with ultrapure water/methanol for three times, and dried under vacuum at 100 °C overnight.

2.2.2. Synthesis of pristine Bi_2S_3 nanosheets

The pristine Bi_2S_3 was prepared by the similar procedures of M-Bi_2S_3 nanosheet precursor without adding $M(NO_3)_2 \cdot 6$ H_2O in the mixed solution.

2.2.3. Synthesis of SAA-Zn_1Bi, SAA-Mn_1Bi and pristine Bi catalysts

The SAA-Zn_1Bi, SAA-Mn_1Bi and Bi catalyst were then formed in situ by reducing the Zn-Bi_2S_3, Mn-Bi_2S_3 and Bi_2S_3 precursor at a constant voltage of -0.5 V vs. RHE for 30 min in a standard three-electrode flow cell system supplied with CO_2 gas, with 0.5 M $KHCO_3$ as electrolyte.

2.2.4. Preparation of GDEs

10 mg catalyst powder and 50 μL Nafion solution (5 wt%) were first dispersed into 3 mL ethanol under ultrasonication for more than 60 min. The formed catalyst ink was sprayed onto a 2×0.5 cm^2 gas-diffusion carbon paper (Sigracet 29 BC from Fuel Cell Store) to achieve a loading of 1 mg cm^{-2} as the working electrode. Ag/AgCl electrode and Ni foam were respectively used as the reference and counter electrodes to assemble a three-electrode flow cell.

2.3. Characterizations

Powder X-ray diffraction (XRD) patterns of the catalysts were recorded on a Bruker D8 DISCOVER A25 X-ray diffractometer (Germany) with Co K α radiation (3 kV). The electrode after the electrocatalytic test was washed with deionized water firstly to remove the residual potassium hydroxide, then dried, scraped, and collected the spent catalyst powder to exclude the ineradicable XRD diffraction peak of the substrate. Moreover, the same electrocatalytic process was repeated several times to collect enough amount of samples for the XRD measure. The Field-emission scanning electron microscopy (FE-SEM, FEI-Verios G4) operated at 15 KV was carried out to analyze the morphologies of the as-prepared electrocatalysts. The morphology and structure of samples were studied using transmission electron microscopy (TEM, FEI Talos F200X TEM operated at 200 kV). The actual content of Bi and Cu were obtained on an Inductively Coupled Plasma Atomic Emission Spectrometry (ICP-AES, NexION™ 350D PerkinElmer USA). N_2 sorption experiment at -196 °C was tested on a 3 H-2000PS2 type PS2–0790 Surface Area Porosity Analyzer from Beishide Instrument Technology (Beijing) Co., Ltd. The specific surface area and pore volume were calculated from the Brunauer-Emmett-Teller (BET) and Barrett-Joyner-Halenda (BJH) methods, respectively. The ex-situ Raman spectra were obtained on a Raman microscope (Renishaw InVia, UK) using an excitation wavelength at 532 nm. X-ray photoelectron spectroscopy (XPS) analysis was conducted on a Kratos Axis Ultra DLD spectrometer with Al Kα radiation. The X-ray absorption fine structure spectra (Zn and Mn K-edge) were collected at 4B9A beamline in Beijing Synchrotron Radiation Facility (BSRF). The storage rings of BSRF were operated at 2.5 GeV with a stable current of 400 mA. Using Si (111) double-crystal monochromator, the data collection were carried out in transmission mode. All spectra were collected in ambient conditions.

2.4. Electrochemical tests

Electrochemical experiments were performed in a four-part self-made microflow cell and the electrochemical data were recorded on a CS350H electrochemical workstation (Wuhan Corrtest Instruments Corp., Ltd.). The gas-diffusion carbon papers loaded with electrocatalysts (1 mg cm^{-2}) served as the working electrode. Ag/AgCl electrode and Ni foam were used as the reference and counter electrodes, respectively. For electrochemical tests, all the potentials were referred to a RHE based on the equation: E (versus RHE) = E (versus Ag/AgCl) + 0.197 V + 0.059 V × pH. ECSA (Electrochemical Active Surface Area) was detected by the double-layer capacitance (C_{dl}) which was measured from various scan rates CV measurements. The linear slope of the double-layer charging current versus the scan rate plot of curves is equivalent to twice the double-layer capacitance C_{dl}, and the C_{dl} is proportional to the ECSA. The long-term stability was conducted by a custom-made membrane electrode assembly. The cell resistance was determined by performing an electrochemical impedance spectroscopy measurement using a Chi760e electrochemical workstation carried out

from 100 kHz to 0.1 Hz with an amplitude of 5 mV at open-circuit voltage. The potential was manually corrected using Ohm's law: E (versus RHE) = E (versus Ag/AgCl) + 0.197 V + 0.0591 × pH - 0.85 × i × R_s, Where R_s represents the calculated solution resistance.

2.4.1. Electrochemical in situ spectroscopy

The catalyst inks used for in situ ATR-IR and in situ Raman spectroscopy measurements were the same as those for electrochemical measurements.

2.4.2. Electrocatalytic CO_2 reduction in membrane electrode assembly (MEA) electrolyzer

To further get insight into the long-term durability of CDB electrocatalyst, a 5 cm^2 membrane electrode assembly (MEA) electrolyzer with 0.5 M $KHCO_3$ anolyte and humid CO_2 was selected due to its stability at high current density. The MEA was constructed by the cathode, an anion exchange membrane (Fumasep FAB-PK-130), and an RuOx/GDE anode. During the electrochemical stability test, humid CO_2 gas was supplied to the cathode side, and 1 M KOH was fed into the anode side with a flow rate of 10 mL·min^{-1}. To prevent the accumulation of (bi)carbonate on GDL, the anolyte was replaced every 12 h. All applied bath voltage was actual without the ohm-correction in MEA electrolyzer.

2.4.3. MEA-SSE

For the two-electrode cells with the solid proton conductor for pure formic acid solution production [7], an anion exchange membrane (Fumasep FAB-PK-130) and a cation exchange membrane (Nafion 115) were used for exchange of HCOO$^-$ and H$^+$, respectively. Around 1 mg cm^{-2} Zn-Bi_2S_3 loaded on the Sigracet 35 BC electrode (5 cm^2 electrode area) was used as a cathode, and RuO_2 loaded on a titanium mesh as an anode. A humidified CO_2 gas flow (30 mL min^{-1}) was fed to the cathode side and an aqueous solution of H_2SO_4 (0.5 M) was circulated around the anode side. The porous solid Dowex 50WX8 ion-exchange resin (50–100 mesh) was employed as the HCOO$^-$ conductor, which was filled in the middle channel (2.5 cm × 2.5 cm, 3 mm thick). Deionized water with a flow rate of 25 mL h^{-1} was used to release the HCOOH produced within the solid electrolyte layer. All applied bath voltage was actual without the ohm-correction in MEA-SSE electrolyzer.

2.4.4. Electrocatalytic performance and product analysis

Before the CO_2RR test, the CO_2 gas (99.99%) was first purged into the cathode chamber with 1.0 M KOH electrolyte for 30 min. Under the same conditions, the electrolysis process and linear sweep voltammetry (LSV) with a scan rate of 20 mV s^{-1} were also tested with a continuous bubbling of CO_2 gas at a flow rate of 30 sccm. The catholyte was continuously circulated at a rate of 10 sccm. The gas products in the cathodic chamber were vented directly into the gas sampling loop of gas chromatography (GC 7920) and the separated gas products were analyzed by a thermal conductivity detector (TCD) (H_2) and a flame ionization detector (FID) with methane reformer (CO). Nitrogen was employed as the carrier gas.

2.4.5. Calculation of faradaic efficiency

The Faradaic efficiency of CO and H_2 can be calculated using the following equation:

$$FE(100\%) = \frac{Q_{CO} \text{or} Q_{H_2}}{Q_{tot}} \times 100\% = \frac{C \times \text{flowrate} \times N \times F}{V_m \times J_{total}} \times 100\% \quad (1)$$

Where C is the concentration detected by the GC, N is the number of a molecule for desired outcomes, F is the Faraday constant (96,500 C mol^{-1}), V_m is the molar volume of gas when the temperature is 298 K and J_{total} is the steady-state current.

Liquid products were detected using a Bruker Avance 400 MHz NMR spectrometer. Typically, 0.4 mL collected catholyte was mixed with 100 μL D_2O and 20 ppm dimethyl sulfoxide as the internal standard, and

the corresponding Faradaic efficiency can be calculated as below:

$$FE(100\%) = \frac{\alpha n F}{Q} \quad (2)$$

where α is the number of electrons required to form targeted products (e. g., α = 2 for reduction CO_2 to HCOOH or CO); Q is the total charge passed during the specified time.

2.5. In situ experiments

2.5.1. In situ ATR-IR measurements

The in situ ATR-IR test was conducted following a previously reported procedure with a slight modification [32] (Fig. S33). The catalyst ink were droped on a 2 × 2 cm^2 carbon paper to prepare the working electrode (1 mg catalyst / cm^2). Before the in situ ATR-IR test, the electrode underwent potential cycling in 0.5 M $KHCO_3$ by cyclic voltammetry between − 2.5–0 V (vs. Ag/AgCl) with 10 mV s^{-1} until stable voltammograms were obtained. Additionally, Pt was used as a counter electrode, and Ag/AgCl was used as a reference electrode. Subsequently, the electrode was immersed in a 30 mL electrolyte containing 0.5 M $KHCO_3$ in the spectra electrochemical setup. CO_2 or argon was bubbling to the electrolyte in advance and continuously bubbled throughout the experiment. The IR test was conducted by ThermoFisher scientific iS50 with a liquid N_2-cooled MCT (mercury cadmium telluride) detector using a VeeMax III ATR accessory (Pike Technologies). The obtained carbon paper was fixed above the Si crystal and connected with a glassy carbon electrode. A CHI 760E electrochemical workstation (CH Instruments, USA) was connected for chronoamperometric tests from − 0.2 to − 1.5 V vs. RHE stepwise. The spectra under open circuit potential (OCP) were recorded for comparison.

2.5.2. In situ Raman measurements (for structural evolution of M-Bi_2S_3 and Bi_2S_3 precursor)

50 μL of catalyst ink was uniformly deposited on a screen-printed working electrode (Pine Research Instrumentation, RRPE1002C) with a diameter of 5 mm. The fully dried electrode was connected to the 760E electrochemical workstation via a cell grip and USB connector and was then attached to a microscope slide on the sample stage. 50 μL of 1 M CO_2-bubbled KOH electrolyte was added dropwise to the electrode. A coverslip was then placed on the top of the electrode. In situ Raman spectra were collected using a Raman spectroscope (HORIBA LabRAM HR Evolution) configured with an MPLN50x objective len (Olympus) and a 532 nm Raman laser. Baseline correction was applied in all in situ Raman spectra. All applied potentials were converted to RHE.

2.5.3. In situ Raman measurements (for mechanism investigation)

The measurement was carried out by utilizing a home-made spectroelectrochemical flow cell (Fig. S34) through a quartz window to detect the cathode GDL. A piece of catalysts supported on GDL (2 × 2 cm^2, loading mass: 1.0 mg cm^{-2}) was inserted through the wall of the cell to keep the plane of the working electrode perpendicular to the incident laser. The reference electrode was Ag/AgCl (saturated KCl) placed in the cathodic compartment; the counter electrode was a graphite rod placed in the anodic compartment. A syringe pump was used to pump 1 M KOH at a constant flow rate of 5 mL min^{-1} over the GDL. Raman spectra were obtained at 5 min after the potential was initially applied. Potential-dependent spectra were obtained at OCP, − 0.1, − 0.3, − 0.5, − 0.7, − 0.9, − 1.1 and − 1.3 V vs RHE.

2.6. Density functional theory methods

First Principles calculations were performed using the Vienna ab initio simulation package [33] (VASP) in the framework of density functional theory (DFT) with projector augmented wave pseudopotentials. The Perdew-Burke-Ernzerhof functional was adopted to describe

the exchange-correlation function based on the generalized gradient approximation [34]. Spin polarization was included in the calculations. The energy cutoff for plane wave basis was set to 500 eV in conjunction with the Gamma-centered Monkhorst-Pack scheme for k-point sampling [35]. A $10 \times 10 \times 5$ k-point sampling was used for bulk lattice constants optimization for Bi, while a $3 \times 2 \times 1$ k-point sampling was used for studying the CO_2RR mechanism on the (012) surfaces of Bi-based systems. In the vertical direction, a vacuum layer 15 Å thick was introduced for all the surfaces, which ensured no interaction between the periodic images of the slabs. The convergence criterion of the total energy was set to 10^{-5} eV. A Gaussian smearing of 0.2 eV was adopted for the electronic temperature to speed up the calculation convergence. For geometric optimizations, all ions were relaxed to a force tolerance of less than 0.01 eV/ Å. DFT-D3(BJ) functional method was also taken into account [36]. The pictorial representations of the atomic structures were prepared using the Visualization for Electronic and Structural Analysis (VESTA). The computational hydrogen electrode model [37] proposed by Nørskov et al. was used to calculate each elementary reaction's potential free energy changes. The free energy of $(H^+ + e^-)$ pair in the elementary electrochemical steps equals half of the free energy of gaseous H_2 at an applied potential U = 0 V versus RHE for all pH. The equilibrium potential for the reaction $CO_2 + 2(H^+ + e^-) \rightarrow HCOOH$ is calculated to be -0.19 V. The Gibbs free energy change of different steps was calculated as follows:

$$\Delta G = \Delta E + \Delta ZPE + T\Delta S$$

Where the ΔE, ΔZPE and ΔS is the changes in the system energy calculated from the DFT, zero-point energy and the calculated entropy, respectively. T is the standard temperature of 298.15 K.

The binding energies (E_b) of all adsorbed species were calculated as follows:

$$E_b = E_{tot} - E_{sur} - E_{spe}$$

Where the E_{tot} is the total energy of the slab with adsorbate systems, E_{sur} is the energy of the Bi-based slab and the E_{spe} is the energy of adsorbed species.

2.7. Grey correlation analysis

Grey correlation analysis theory is a multi-factor statistical analysis method [38]. Compared with the traditional multi-factor analysis method, grey correlation analysis can obtain the correlation degree between factors under less data conditions [39]. The greater the correlation, the greater the correlation value, and the more sensitive the reference factors are to comparison factors. In this work, the adsorption energy of different intermediate products to be analyzed is determined as the reference sequence, and the overpotential of CO_2RR is taken as the comparison sequence. Take the matrix data composed of the reference sequence and comparison sequence for dimensionless processing to eliminate the impact of the difference of each indicator unit and the magnitude of the difference between the numerical values. Then calculate the correlation coefficient to obtain the grey correlation degree.

3. Results and discussion

3.1. Theoretical calculations

Considering the cost issue and the diversity of metal atoms, nine typical types of metal of 3d transition group were selected as foreign metal atoms to construct Bi-based single atom alloys (SAA-X_1Bi, X = Sc, Ti, V, Mn, Fe, Co, Ni, Cu, and Zn), and first-principle calculations were performed to explore the CO_2RR activity of the nine SAA-X_1Bi and pristine Bi electrocatalysts. In general, after the adsorption and activation of CO_2 on the surface of the electrocatalysts, the first hydrogenation

step will generate three possible intermediates [40]: *OCHO, *COOH, and *H, which dominate the final product is formate (*OCHO), other C_1 and C_{2+} products (*COOH), and H_2 (*H), respectively. The Gibbs free energy (ΔG) calculation results reveal that $\Delta G(*OCHO)$ lower than $\Delta G(*COOH)$ and $\Delta G(*H)$, suggesting that the CO_2RR reaction occurred on the surfaces of Bi and all SAA-X_1Bi catalysts is more favorable to form *OCHO intermediate (Fig. 1b, Fig. S1, and Fig. S2). This indicates that formate will be the main product when all the SAA-X_1Bi and Bi electrocatalysts are used in CO_2RR.

The free energy diagram of the CO_2RR performance of the nine SAA-X_1Bi and Bi catalysts, including the two-electron transfer of CO_2 to CO and HCOOH, was constructed (Fig. 1a). The first vital step for the CO_2RR transformation is the activation of the inert CO_2 molecule [7], the binding energy of CO_2 on the Bi surface is -0.19 eV, manifesting a weak interaction. In contrast, most SAA-X_1Bi can strengthen the interaction with CO_2 except for the V_1Bi catalyst (-0.14 eV) (Fig. S3 and Table S1). Furthermore, among various SAA-X_1Bi systems with enhanced CO_2 adsorption ability, SAA-Mn_1Bi (-1.33 eV) and SAA-Fe_1Bi (-0.76 eV) induce strong chemical interaction with CO_2 while the others maintain a weak enhanced interaction behavior, ranging from -0.21 eV to -0.35 eV. The enhanced adsorption ability of SAA-X_1Bi towards CO_2 is beneficial to activate CO_2 and facilitates further reduction reaction[7]. As the discussion above, SAA-X_1Bi catalysts prefer to form *OCHO intermediate and further couple with proton and electrons to generate formic acid. Based on the calculation of the thermodynamic reaction energy barrier of $G_1[\Delta G(CO_2(g) - *CO_2)]$, $G_2[\Delta G(*CO_2 - *OCHO)]$, $G_3[\Delta G(*OCHO - *HCOOH)]$ and $G_4[\Delta G_{desorption}(*HCOOH)]$ of the ten catalysts, SAA-Zn_1Bi (-0.21 V) and SAA-Cu_1Bi (-0.37 V) exhibit lower limiting potential than pristine Bi materials (-0.42 V), while other SAA-X_1Bi catalysts show higher limiting potential than that of pristine Bi materials, ranging from -0.47 V to -1.26 V (Table S2). SAA-Zn_1Bi electrocatalyst displays the best regulation effect with an ultra-low limiting potential among the ten catalysts.

To further understand the activation behavior of SAA-X_1Bi catalysts, we introduced the gray correlation analysis method [41] to elaborate the relationship between the adsorption behavior of intermediate and the limiting potential. According to the analysis of the grey correlation coefficient (Fig. S4), limiting potential emanates an intimate correlation with the adsorption energy of *OCHO since it possesses the biggest grey correlation degree of 0.94. Then, the limiting potential of the catalysts for each elementary step ($\Delta G_1, \Delta G_2, \Delta G_3, \Delta G_4$) can be estimated according to the catalyst's affinity for OCHO (Fig. S5 and Table S2), and the most negative U_L determines the theoretical overpotential ($U_L - E_{equilibrium\ potential}$). From Fig. 1c, the reduction processes of $CO_2(g) - *CO_2$, $*OCHO - *HCOOH$ and the desorption of *HCOOH gradually become the limiting reaction step as the increased strength of *OCHO, respectively. Too strong affinity towards OCHO intermedia (i.e., SAA-Mn_1Bi) will cause a difficult desorption process of HCOOH. On the other hand, too weak affinity (i.e., Pristine Bi) will make the adsorption and activation of the CO_2 molecule become a limiting step. SAA-Zn_1Bi catalyst with a moderate adsorption energy of *OCHO sits near the top of this "volcano" type relation, implying the best catalytic ability to generate formic acid since the moderate adsorption energy for adsorbates makes each pronation step and final desorption more facile compared to other SAA-X_1Bi and pure Bi catalysts.

Since the prominent factor that can produce HCOOH with low limiting overpotential is the moderate adsorption ability towards *OCHO intermedia, the adsorption systems of SAA/OCHO were further analyzed to reveal the origin of the moderate adsorption energy of SAA-Zn_1Bi catalyst. As depicted in Fig. 2a and Fig. S6, there are three different types of adsorption structures when the *OCHO is adsorbed on the catalyst surface. Type I (pristine Bi), Type II (Sc_1Bi, Ti_1Bi, and Mn_1Bi), and Type III (V_1Bi, Fe_1Bi, Co_1Bi, Ni_1Bi, Cu_1Bi, and Zn_1Bi) represent the interaction between the catalysts and OCHO through the single Bi-O bond, double O-foreign metal bonds, and the combination of
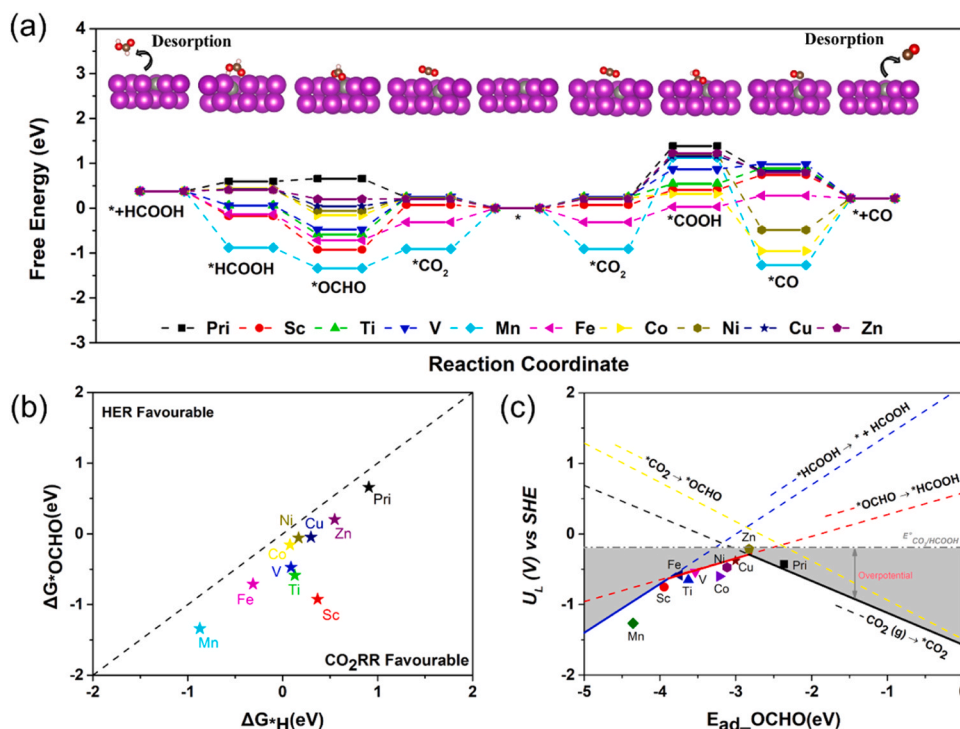
Fig. 1. Theoretical prediction for the best performance SAA catalyst. (a) Free-energy landscape for CO_2 reduction on the surfaces of Bi and SAA catalysts. (b) Calculated Gibbs free energy changes in the first protonation steps for CO_2RR and HER on the surfaces of Bi and SAA catalysts. (c) limiting potentials (U_L) for each elementary steps in the mechanism in Fig. 1a Each line is the calculated potential at which the indicated elementary reaction step is neutral with respect to free energy, as a function of the electrocatalysts' OCHO affinity. The equilibrium potential for the overall electrochemical reduction of CO_2 to HCOOH is − 0.19 V versus RHE. Thermodynamics limits any real catalyst to operate at potentials more negative than the equilibrium potential, therefore, the theoretical overpotential as a function of E_{ad_OCHO} can be represented by the distance between the equilibrium line and the most-negative limiting potential line (highlighted in gray).

Bi-O bond and foreign metal-O bond, respectively, which is also consistent with the partial density of states analysis (Fig. S7). Charge density differences illustrate that electrons transfer from the SAA-X_1Bi or Bi surface to *OCHO group in the adsorption process, mainly concentrating on the region of metal/O. Bader charge analysis (Fig. 2b) reveals that Type II materials possess the most electron transfer during the adsorption process of *OCHO, and the electron transfer of type I and type III is close.

Next, we selected representative pure Bi (Type I), SAA-Mn_1Bi (Type II) and SAA-Zn_1Bi (Type III) catalysts for further electronic structure analysis (Fig. 2a), and Integrated Crystal Occupation Hamiltonian Population (ICOHP) was also performed to identify the bond strength between the O (*OCHO) and metal (Bi, Mn, and Zn) in these catalysts. The results (Table S3) indicate that the bond strength of Bi-O (Type I) is greater than Mn-O (Type II) and Zn-O/Bi-O (Type III), which seems to be contrary to the trend of calculated adsorption energy, indicating there must be other factors affecting the adsorption energy. Analyzing the surface structure of the three types of catalysts before and after adsorption (Fig. 2c), one intriguing phenomenon can be seen that there is atomic structure distortion in SAA-Mn_1Bi, while this distortion is less in SAA-Zn_1Bi and not in pure Bi. However, these distortions will be significantly decreased when the OCHO is adsorbed on SAA-Mn_1Bi and SAA-Zn_1Bi surfaces. The decreased atomic structure distortion in SAA-Mn_1Bi and SAA-Zn_1Bi reduces the energy of the total system, which increases the adsorption strength of *OCHO intermedia. Therefore, the adsorption behavior of *OCHO on SAA-X_1Bi is actually affected by both lattice distortion and bonding mode. SAA-Mn_1Bi has enormous adsorption energy due to the significant lattice distortion transformation, while SAA-Zn_1Bi has slightly increased adsorption energy own to the small lattice distortion transformation.

Besides, except desorption, *HCOOH may be further pronation to form *CHO, *HOCHOH, or *H_2COOH intermediates [42], which is the key to forming multi-electrons C1 products such as CH_4 and CH_3OH. Therefore, we further explored the thermodynamic barrier of the pronation of *HCOOH to form these possible intermediates on the surface of the SAA-Zn_1Bi catalyst. As shown in Fig. 2d, the thermodynamic barrier of HCOOH desorption possesses the lowest energy input among these

intermediates, so SAA-Zn_1Bi tends to desorb HCOOH and then suppresses the production of various products. Based on the above calculation research conclusion, we deem that SAA-Zn_1Bi is the most potential conversion SAA electrocatalyst for CO_2 to formic acid.

3.2. Single-atom alloy Bi-based catalysts synthesis and characterization

The SAA-X_1Bi (X = Zn and Mn) and pristine Bi catalysts were fabricated by a two-step in situ electrochemical reduction method (Fig. S8): (1) Zn-Bi_2S_3, Mn-Bi_2S_3, and pristine Bi_2S_3 precursors were prepared by a modified hydrothermal method [20]. (2) the as-obtained precursor was electrochemically reduced in situ to form SAA-X_1Bi catalysts. The properties of Zn-Bi_2S_3, Mn-Bi_2S_3, and pristine Bi_2S_3 precursors and the in situ structural evolution processes are examined and analyzed and the details are shown in Supporting information (Fig. S9-S15). The results of inductively coupled plasma atomic emission spectroscopy (ICP-AES) of the as-formed SAA-Zn_1Bi demonstrate the existence of Zn, and its atomic loading is 3.2% (Table S5), the X-ray photoelectron spectroscopy (XPS) analysis also confirms this conclusion (Fig. S16a). Field-emission scanning electron microscopy (FE-SEM) reveals that SAA-Zn_1Bi maintains the nanosheet-like morphology of its counterpart Zn-Bi_2S_3 precursor (Fig. S17), corresponding energy dispersive X-ray (EDX) elemental mapping of SAA-Zn_1Bi (Fig. 3b and S18c) affirms the uniform distribution of Zn elements in the Bi nanosheet. Besides, the X-ray diffraction (XRD) patterns (Fig. S19a-b) and enlarged Raman spectrum (Fig. S19c) of SAA-Zn_1Bi suggest homogeneous incorporation of Zn atoms. The high-angle annular dark-field scanning transmission electron microscopy (HAADF-STEM) images (Fig. 3c and Fig. S20) indicate the atomic dispersion of Zn in the Bi matrix, which preliminarily verifies the formation of Zn single-atom alloy.

To further investigate the local atomic coordination and electronic structure of the Zn species in the SAA-Zn_1Bi, we performed X-ray absorption near-edge structure (XANES) spectrum measurements using Zn foil and ZnO as reference. As shown in the Zn K-edge XANES spectra (Fig. 3d), the intensity of the white line ($1s \rightarrow 4p$ orbital transition [43]) at Zn K-edge of SAA-Zn_1Bi locates between those of Zn foil and ZnO, indicating that the valence state of the Zn species in SAA-Zn_1Bi is
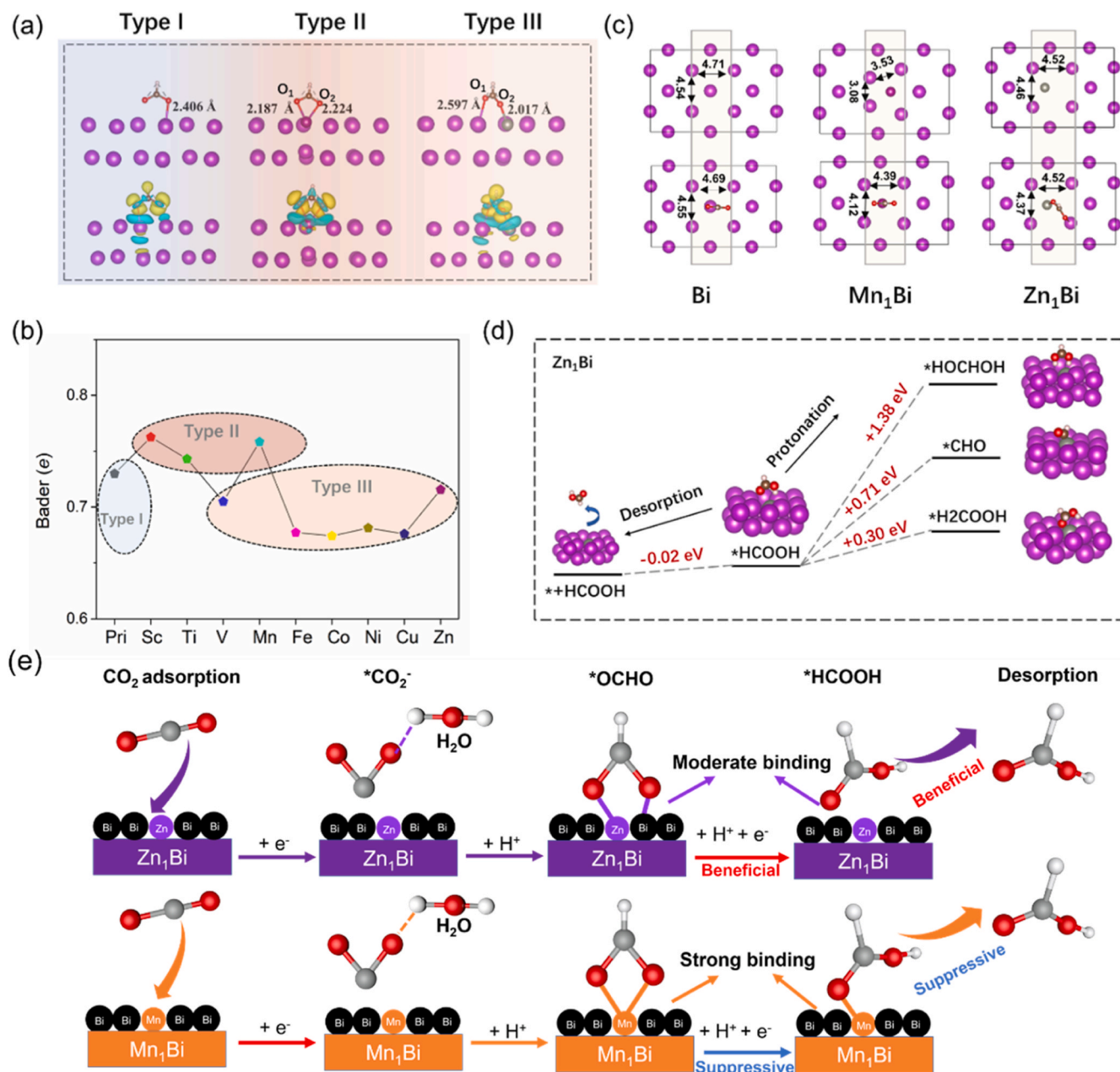
Fig. 2. Catalytic mechanisms in different SAA materials. (a) Three typical catalysts (Type I: Bi, Type II: SAA-Mn_1Bi, Type III: SAA-Zn_1Bi) with *OCHO adsorption. (b) Bader charge analysis of electrons transfer from substrates to *OCHO. (c) Lattice change before and after adsorption of *OCHO on three substrates. (d) Possible intermediates and reduced products for further protonation of *HCOOH on Zn_1Bi. (e) A proposed reaction mechanism for the CO_2RR to formate on SAA-Zn_1Bi and SAA-Mn_1Bi.

probably situated between 0 and + 2. Moreover, the extended X-ray absorption fine structure (EXAFS) spectra (Fig. 3e) and the wavelet-transform analysis (Fig. 3f and Fig. S21) of SAA-Zn_1Bi EXAFS further disclose that only the peaks of the Zn-O bond (at 1.03 Å and 1.56 Å) and Zn-Bi bond (at 2.51 Å) are detected [44,45], and no Zn-Zn bonds are found. The EXAFS fitting results (Fig. S22 and Table S6) further support the wavelet-transform analysis, confirming the successful preparation of SAA-Zn_1Bi electrocatalyst by the in situ electrochemical reduction method. Additionally, the Zn–O bonds may be due to the oxidation of the SAA-Zn_1Bi catalyst during ex-situ tests [7]. Moreover, the two XPS peaks of Bi 4f7/2 and Bi 4f5/2 in the SAA-Zn_1Bi shift to lower energy compared with the pristine Bi (about −0.18 eV, Fig. S16c), implying the lower average oxidation state of Bi atoms, which is attributed to the electron transfer from Zn to Bi atoms in the

SAA-Zn_1Bi due to a larger electronegativity of Bi (1.9) than that of Zn (1.6). Taken together, these results undoubtedly confirm that one Zn single-atom alloyed metallic Bi electrocatalyst is obtained via the in situ structural reconstruction of the Zn-Bi_2S_3 precursor, and there is certain electron interaction between Zn_1 atom and the parent metal Bi. The similar analyses of the SAA-Mn_1Bi also confirm the formation of Mn single atom-alloyed metallic Bi (Fig. S16-S23).

3.3. Electrochemical CO_2 reduction performance

To verify the accuracy of the predicted conclusions of theoretical calculations, we evaluated the electrocatalytic performance of SAA-Zn_1Bi, SAA-Mn_1Bi, and pristine Bi catalysts in a flow cell system (Fig. S24) using 1.0 M KOH at different cathodic potentials. Linear
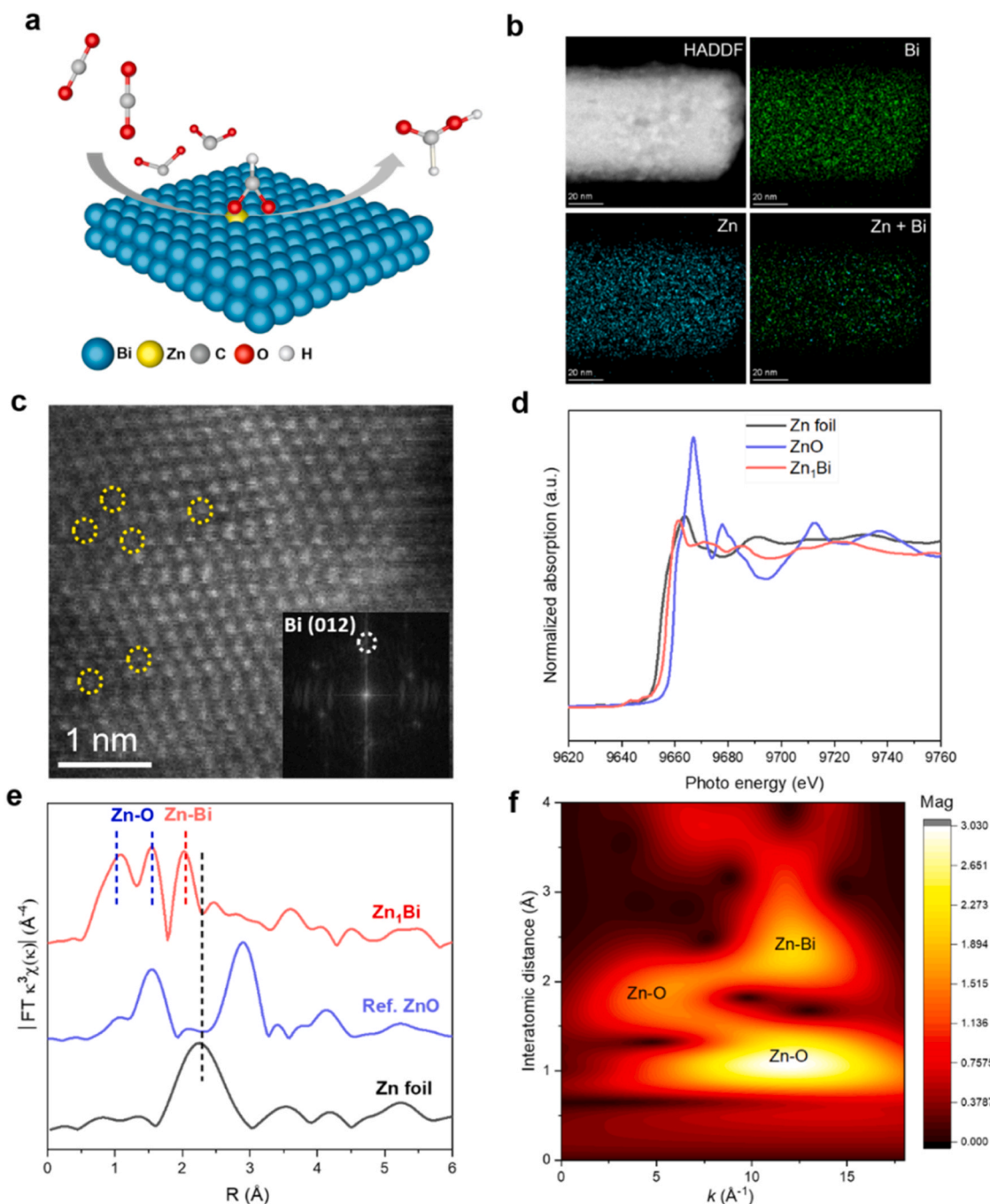
Fig. 3. Characterizations of Zn sites in the SAA-Zn_1Bi catalyst. (a) Schematic illustration of CO_2 conversion into HCOOH over the SAA-Zn_1Bi catalyst. (b) STEM-EDS mapping of the SAA-Zn_1Bi catalyst. (c) Aberration-corrected HAADF-STEM images of the SAA-Zn_1Bi catalyst and corresponding FFT pattern. The yellow circle highlights the single-dispersed Zn atom. (d) Zn K-edge XANES and (e) corresponding k^3-weighted Fourier transform of EXAFS spectra of SAA-Zn_1Bi, ZnO, and Zn foil. (f) Wavelet-transform analysis of EXAFS spectrum of SAA-Zn_1Bi.

sweep voltammetry (LSV) curves (Fig. 4a) illustrate that the SAA-Zn_1Bi electrocatalyst achieves a larger cathodic current density and a more positive onset reduction potential (-0.26 V_{RHE}) in the CO_2-fed flow cell than SAA-Mn_1Bi and Bi, demonstrating its superior CO_2RR activity. Moreover, the potentiostatic electrolysis at step potentials (Fig. 4b) exhibits the formate is the dominant product for the three catalysts (Fig. S25a-b), which benefits from their favorable adsorption to the *OCHO intermediate obtained by the DFT calculations. For the SAA-Zn_1Bi electrocatalyst, the maximum formate FE of 96.5% can be achieved at -0.75 V_{RHE} and the formate partial current density ($j_{formate}$) can reach up to ~700 mA cm^{-2} at -0.86 V_{RHE} (Fig. 4c), obviously

higher than that of other SAA-X_1Bi and pristine Bi catalysts. A high plateau of formate FE over 90% is retained across a broad potential range from -0.35 to -1.45 V_{RHE} (1100 mV, Fig. S25c). Notably, the $j_{formate}$ reaches as high as -1323 mA cm^{-2} at -0.86 V_{RHE} (Fig. 4c) and the formate formation rate achieves 24.5 mmol·h^{-1}·cm^{-2} in 5.0 M KOH (Fig. S25d), outperforming all of the reported formate-selective electrocatalysts (Fig. 4d and Table S4). In addition, the effect of Zn content on the catalytic performance of CO_2RR was also studied (Fig. S26), the results showed that only highly dispersed SAA-Zn_1Bi showed the best performance, and the decrease of $j_{formate}$ for the ZnBi catalysts with increased Zn contents is due to the aggregation of Zn species (Fig. S27).
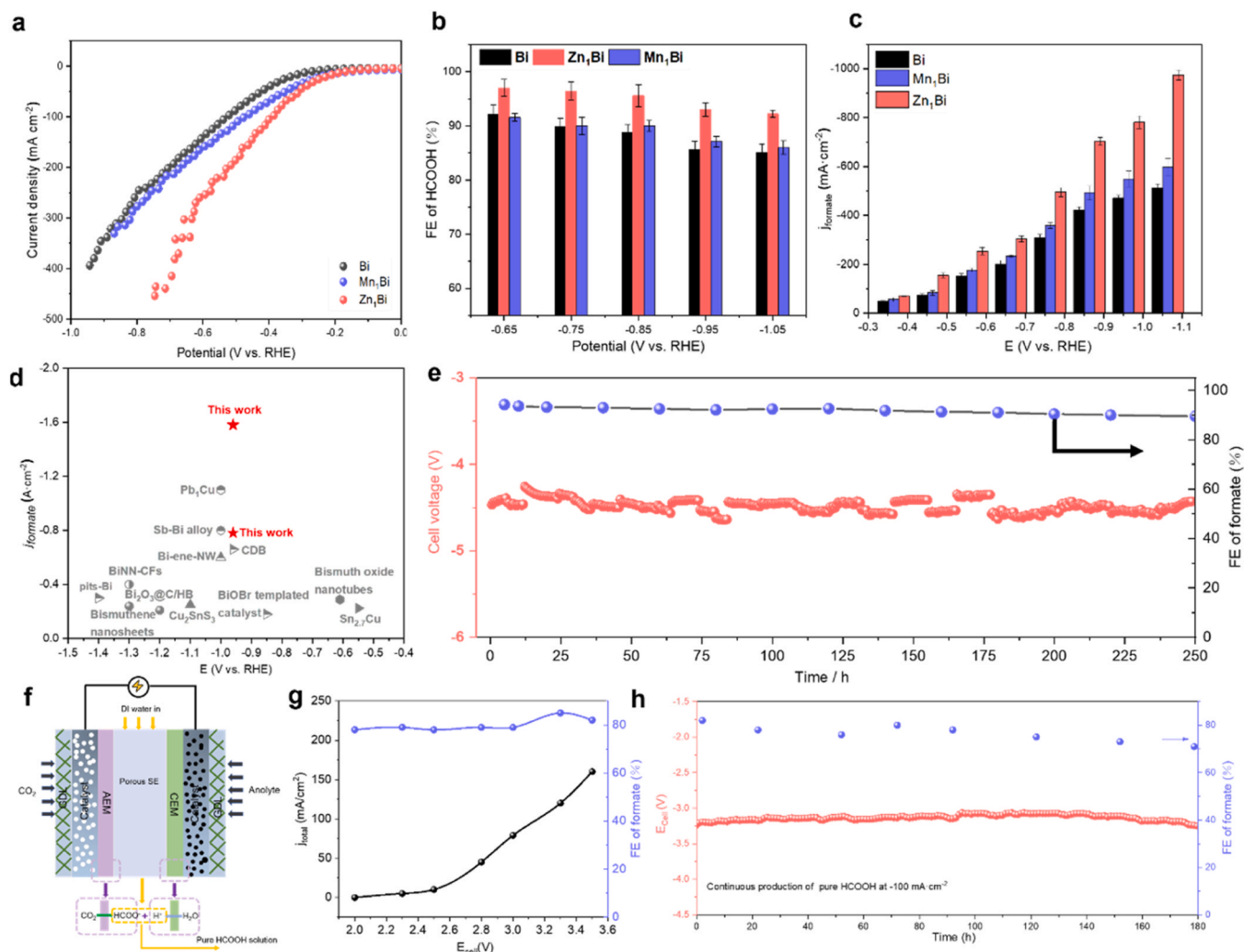
Fig. 4. Electrochemical carbon dioxide reduction measurements. (a) Cathodic polarized curves of SAA-Zn_1Bi, SAA-Mn_1Bi, and Bi in 1.0 M KOH electrolytes. (b) Potential-dependent FE of formate for three catalysts at the potential of − 0.65 V to − 1.05 V. (c) formate partial current densities at different electrolytic potentials in 1.0 M KOH electrolyte with SAA-Zn_1Bi, SAA-Mn_1Bi, and Bi electrocatalysts. (d) Performance comparison of SAA-Zn_1Bi electrocatalyst with the reported electrocatalysts towards CO_2RR to formate in the flow cell. (e) Continuous 250 h electrolysis in a 5 cm^2 MEA electrolyzer under a constant total current density of − 400 mA cm^{-2}. (f) Schematic illustration of the solid-electrolyte cell for CO_2RR to pure formic acid solution. (g) The current density at different cell voltages over the Zn-Bi_2S_3-derived catalyst in the solid-electrolyte cell. (h) The FE and the cell voltage in the long-term stability test for the Zn-Bi_2S_3-derived catalyst at a constant current density of 100 mA cm^{-2}. The error bars in Fig. 4b-c represented the standard deviations of three independent measurements.

Which further confirms the superiority of SAA-Zn_1Bi electrocatalyst due to its unique geometric and electronic structures as disclosed in DFT calculations.

Involving the practical application of CO_2RR, the stability of electrocatalysts is another important factor. Therefore, the long-term electrochemical test of the SAA-Zn_1Bi catalyst was further examined in a 5-cm^2 membrane electrode assembly (MEA) electrolyzer (Fig. S28) with 1 M KOH analyte and humid CO_2. At a current density of − 400 mA cm^{-2}, the SAA-Zn_1Bi catalyst displays an outstanding electrochemical stability of > 250 h continuous operation with stable $FE_{formate}$ (Fig. 4e), which was the best-reported stabilities of CO_2 electroreduction to formate at such harsh conditions (Table S7). Notably, the post-catalysis characterizations reveal that the fully isolated dispersion of Zn atoms among the Bi can be well maintained even after a 50 h and 250 h stability test (Fig. S29).

In addition, to avoid the energy-intensive downstream separation of the formate product from a generated electrolyte with the dissolved salts [46], we employed a solid-electrolyte cell (Fig. 4f and S30) to directly generate pure HCOOH. A peak formate FE of 83% is achieved and the overall current density can reach over 110 mA cm^{-2} at a cell voltage of

3.3 V (Fig. 4 g). No liquid products are observed other than HCOOH by ^{1}H and ^{13}C NMR (Fig. S30c-d). Besides, our all-solid-state cell demonstrates an impressive stability of ~180 h continuous production of 0.13 M (~4.5 L) pure formic acid product (Fig. 4h). Overall, the highly active and selective SAA-Zn_1Bi catalyst offers promising scalability of practical application in electroreduction CO_2 to formate.

The electrochemical double-layer capacitance (C_{dl}) of SAA-Zn_1Bi (2.2 mF cm^{-2}) is higher than that of pure Bi (1.8 mF cm^{-2}) and SAA-Mn_1Bi (1.9 mF cm^{-2}), indicating the generation of abundant active sites on SAA-Zn_1Bi for enhancing electrocatalytic activity (Fig. S31). Moreover, the $j_{formate}$ normalization by ECSA of SAA-Zn_1Bi, SAA-Mn_1Bi, and Bi are − 12.8, − 10.4, and − 9.2 mA cm^{-2}, respectively, demonstrating the higher intrinsic activity for formate synthesis of the SAA-Zn_1Bi electrocatalyst (Fig. S32). The smallest value of 114 mV dec^{-1} at the SAA-Zn_1Bi electrode in comparison with those of SAA-Mn_1Bi (143 mV dec^{-1}) and Bi (173 mV dec^{-1}) (Fig. S33a) indicates that improved electron transfer process of formate production on SAA-Zn_1Bi, highlighting the critical role of isolated Zn atoms in boosting CO_2-to-HCOOH conversion [28]. Furthermore, based on the diameter of semicircular Nyquist plots, the SAA-Zn_1Bi catalyst shows a charge-transfer resistance

(R_{ct}) of 2.7 Ω, lower than that of SAA-Mn$_1$Bi (4.8 Ω) and Bi (5.9 Ω), proving the better electronic conductivity and a fast charge transfer rate of SAA-Zn$_1$Bi electrocatalyst (Fig. S33b).

3.4. The investigation of reaction pathway and the role of *OCHO adsorption in CO$_2$RR

In words, the SAA-Zn$_1$Bi electrocatalyst exhibits remarkable performance and long-term stability for CO$_2$RR to formate, representing the best performance reported to date in our best knowledge, which coordinates with the results of the above DFT forecast. To further verify the explanation of the exceptional capacity for CO$_2$RR to formate of SAA-Zn$_1$Bi electrocatalyst, in situ Attenuated Total Reflectance Infrared (ATR-IR) spectroscopy (Fig. 5 and S34) and in situ Raman spectroscopy (Fig. S35) were conducted. As shown in the spectrum of ATR-IR (Fig. 5), the peak at 1635 cm^{-1} in all three catalysts is assigned to water [21,47]. Compared with the barely observed surface-bound unidentate carbonate species (*CO$_3$) [48–50] at ca. 1520 cm^{-1} in SAA-Zn$_1$Bi catalyst across the entire potential range (Fig. 5a), the *CO$_3$ species intensity of SAA-Mn$_1$Bi is more obvious (Fig. 5b). Moreover, three small bands in the wavenumber range between 2750 and 2900 cm^{-1} as the fingerprint of C-H stretching vibration of *OCHO intermediates [21,51,52] are only detected on SAA-Mn$_1$Bi (Fig. 5b and 5d), suggesting the more difficulty of *OCHO intermedia further hydrogenate to the HCOO$^-$ species on SAA-Mn$_1$Bi in the range of testing potentials, which matches well with the theoretical trend of ΔG_3 (Table S2, SAA-Mn$_1$Bi (0.46 eV) > Bi (0.20 eV) > SAA-Zn$_1$Bi (−0.06 eV)). This results in the characteristic IR band intensities of bidentate HCOO$^-$ species [7,53] at near 1394 cm^{-1} on SAA-Mn$_1$Bi is lower than that of SAA-Zn$_1$Bi although the desorption of *HCOO is more difficult on the surface of SAA-Mn$_1$Bi. Furthermore, the intensity of the bidentate HCOO$^-$ species band on SAA-Zn$_1$Bi

increase progressively as the applied potential scanned more negatively, implying the enhanced *HCOO coverage on the surface of SAA-Zn$_1$Bi, which is consistent with the trend of formate formation rates. In addition, the barely visible signals related to *H$_2$O, *CO$_3$, and HCOO$^-$ species over pristine Bi (Fig. 5c) imply the weak adsorption toward CO$_2$ and subsequent poor electrocatalytic conversion efficiency for CO$_2$RR, as the results given by the DFT calculations. Noteworthily, no typical peaks located at 2000 ~ 2200 cm^{-1}, corresponding to the CO* [7], are detected during the electrocatalytic process, demonstrating the negligible generation of CO on the three catalysts (Fig. S25b).

For the in-situ Raman spectroscopy (Fig. S35), the symmetric stretch vibrations around 1340 and 1590 cm^{-1} can be attributed to the carbon from the GDE, and the peak at 1070 cm^{-1} corresponds to CO$_3^{2-}$ in the electrolyte formed by the dissolution of CO$_2$ [54]. The O–C–O symmetric vibration stretching peaks in bidentate *OCHO [20,55] appear at a more positive potential on SAA-Mn$_1$Bi (−0.7 V$_{RHE}$, Fig. S35a) with a more pronounced intensity than SAA-Zn$_1$Bi and pristine Bi (Fig. S35b-d), implying more accumulation of *OCHO on SAA-Mn$_1$Bi, further confirming the Mn atom-alloyed Bi sites can inhibit the formation of formate due to the strong adsorption of *OCHO intermediates, which is consistent with the in-situ IR results and DFT calculations.

4. Conclusion

In this work, the facts that affect the catalytic properties of Bi-based SAAs electrocatalysts in CO$_2$RR were elaborately uncovered by DFT calculations and grey correlation analysis to guide the construction of outstanding catalysts for CO$_2$RR to formate. Calculation results revealed that the reduction processes of $CO_2(g) - *CO_2$, $*OCHO - *HCOOH$ and the desorption of *HCOOH became the limiting reaction step in turn as the increased strength of *OCHO, and SAA-Zn$_1$Bi was regarded as the
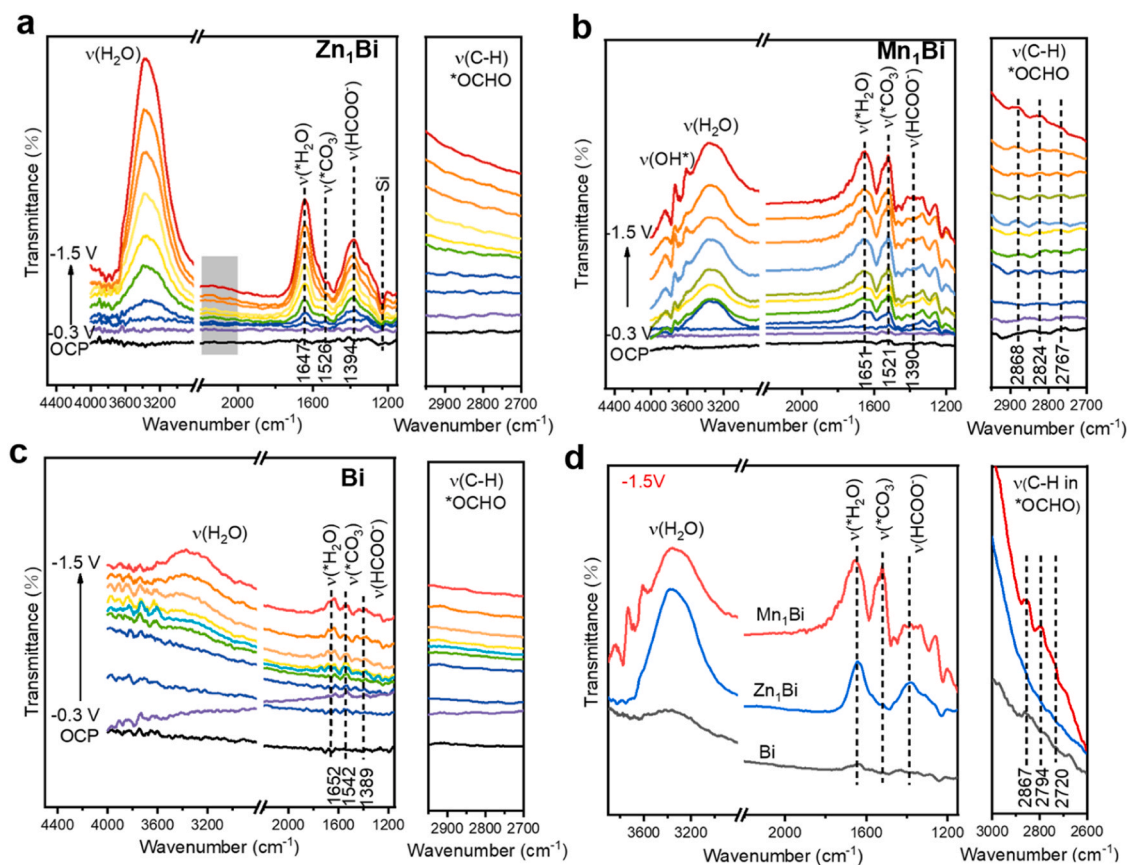

Fig. 5. In situ ATR-IR characterizations. In situ ATR-IR spectra during the electrochemical CO$_2$ reduction for the Zn$_1$Bi (a), Mn$_1$Bi (b) and pristine Bi electrocatalyst (c) in a potential window − 0.2 V to − 1.5 V$_{RHE}$. (d) The ATR-IR spectra for the SAA-Zn$_1$Bi, SAA-Mn$_1$Bi and pristine Bi electrocatalyst at − 1.5 V$_{RHE}$.

best Bi-based SAAs electrocatalysts for CO_2RR to formate due to its ultralow limiting potential and moderate adsorption energy for *OCHO intermediate. The experimental results verified the correctness of the calculations forecast, SAA-Zn_1Bi displayed an industrial-compatible ampere-level current density and remarkable durability for the CO_2RR to formate/formic acid. This work provides new insights into the design and synthesis of high current density and durability SAAs electrocatalysts for CO_2RR.

CRediT authorship contribution statement

T.W. and **H.Z.** conceived the idea. **H.Z.**, **T.W.** and **Q.Z.** supervised the project. **H.S.** and **H.J.** prepared the catalysts and performed the catalytic tests. **T.W.** contributed to the DFT calculations and data analysis. **H.S.**, **H.J.**, **P.Z.**, **Y.F.** and **Z.C.** performed the catalyst characterizations. **H.S.**, **P.Z.**, **Y.C.** and **Y.G.** performed the EXAFS measurements. **H.S.** and **P.Z.** performed the in situ measurements. **H.S.**, **T.W.** and **H.Z.** wrote the paper with input from all authors. All authors discussed the results and commented on the manuscript.

Declaration of Competing Interest

The authors declare that they have no known competing financial interests or personal relationships that could have appeared to influence the work reported in this paper.

Data Availability

The data that support the findings of this study are available from the corresponding authors upon reasonable request.

Acknowledgments

Appendix A. Supporting information

Supplementary data associated with this article can be found in the online version at doi:10.1016/j.apcatb.2023.123140.

References

[1] P. Zhu, H. Wang, High-purity and high-concentration liquid fuels through CO_2 electroreduction, Nat. Catal. 4 (2021) 943–951.

[2] S. Chu, Y. Cui, N. Liu, The path towards sustainable energy, Nat. Mater. 16 (2017) 16–22.

[3] B.J. Currie, M. Kaestli, A global picture of melioidosis, Nature 529 (2016) 290–291.

[4] C. Chen, J.F.K. Kotyk, S.W. Sheehan, Progress toward commercial application of electrochemical carbon dioxide reduction, Chem 4 (2018) 2571–2586.

[5] Z. Myslikova, K.S. Gallagher, Mission Innovation is mission critical, Nat. Energy 5 (2020) 732–734.

[6] E.E. Benson, C.P. Kubiak, A.J. Sathrum, J.M. Smieja, Electrocatalytic and homogeneous approaches to conversion of CO_2 to liquid fuels, Chem. Soc. Rev. 38 (2009) 89–99.

[7] T. Zheng, C. Liu, C. Guo, M. Zhang, X. Li, Q. Jiang, W. Xue, H. Li, A. Li, C.-W. Pao, Copper-catalysed exclusive CO_2 to pure formic acid conversion via single-atom alloying, Nat. Nanotechnol. 16 (2021) 1386–1393.

[8] Y.-J. Ko, J.-Y. Kim, W.H. Lee, M.G. Kim, T.-Y. Seong, J. Park, Y. Jeong, B.K. Min, W.-S. Lee, D.K. Lee, H.-S. Oh, Exploring dopant effects in stannic oxide nanoparticles for CO_2 electro-reduction to formate, Nat. Commun. 13 (2022) 2205.

[9] A. Zhang, Y. Liang, H. Li, B. Zhang, Z. Liu, Q. Chang, H. Zhang, C.-F. Zhu, Z. Geng, W. Zhu, In-situ surface reconstruction of InN nanosheets for efficient CO_2 electroreduction into formate, Nano Lett. 20 (2020) 8229–8235.

[10] J. Duan, T. Liu, Y. Zhao, R. Yang, Y. Zhao, W. Wang, Y. Liu, H. Li, Y. Li, T. Zhai, Active and conductive layer stacked superlattices for highly selective CO_2 electroreduction, Nat. Commun. 13 (2022) 2039.

[11] J. Huang, X. Guo, X. Huang, L. Wang, Metal (Sn, Bi, Pb, Cd) in-situ anchored on mesoporous hollow kapok-tubes for outstanding electrocatalytic CO_2 reduction to formate, Electrochim. Acta 325 (2019), 134923.

[12] B. Wulan, L. Zhao, D. Tan, X. Cao, J. Ma, J. Zhang, Electrochemically driven interfacial transformation for high-performing solar-to-fuel electrocatalytic conversion, Adv. Energy Mater. (2022), 2103960.

[13] Y. Yuan, Q. Wang, Y. Qiao, X. Chen, Z. Yang, W. Lai, T. Chen, G. Zhang, H. Duan, M. Liu, In situ structural reconstruction to generate the active sites for CO_2 electroreduction on bismuth ultrathin nanosheets, Adv. Energy Mater. (2022), 2200970.

[14] B. Ren, G. Wen, R. Gao, D. Luo, Z. Zhang, W. Qiu, Q. Ma, X. Wang, Y. Cui, L. Ricardez–Sandoval, A. Yu, Z. Chen, Nano-crumples induced Sn-Bi bimetallic interface pattern with moderate electron bank for highly efficient CO_2 electroreduction, Nat. Commun. 13 (2022) 2486.

[15] L. Lin, X. He, X.G. Zhang, W. Ma, B. Zhang, D. Wei, S. Xie, Q. Zhang, X. Yi, Y. Wang, A nanocomposite of bismuth clusters and $Bi_2O_2CO_3$ sheets for highly efficient electrocatalytic reduction of CO_2 to formate, Angew. Chem. 135 (2023), e202214959.

[16] Z. Niu, X. Gao, S. Lou, N. Wen, J. Zhao, Z. Zhang, Z. Ding, R. Yuan, W. Dai, J. Long, Theory-guided S-defects boost selective conversion of CO_2 to HCOOH over In_4SnS_8 nanoflowers, ACS Catal. (2023) 2998–3006.

[17] Q. Zhu, D. Yang, H. Liu, X. Sun, C. Chen, J. Bi, J. Liu, H. Wu, B. Han, Hollow metal–organic-framework-mediated in situ architecture of copper dendrites for enhanced CO_2 electroreduction, Angew. Chem. 132 (2020) 8981–8986.

[18] F. Yang, A.O. Elnabawy, R. Schimmenti, P. Song, J. Wang, Z. Peng, S. Yao, R. Deng, S. Song, Y. Lin, M. Mavrikakis, W. Xu, Bismuthene for highly efficient carbon dioxide electroreduction reaction, Nat. Commun. 11 (2020) 1088.

[19] J. Zhang, T. Fan, P. Huang, X. Lian, Y. Guo, Z. Chen, X. Yi, Electro-reconstruction-induced strain regulation and synergism of Ag-In-S toward highly efficient CO_2 electrolysis to formate, Adv. Funct. Mater. 32 (2022), 2113075.

[20] H. Shen, Y. Zhao, L. Zhang, Y. He, S. Yang, T. Wang, Y. Cao, Y. Guo, Q. Zhang, H. Zhang, In-situ constructing of copper-doped bismuth catalyst for highly efficient CO_2 electrolysis to formate in ampere-level, Adv. Energy Mater. 13 (2023), 2202818.

[21] T. Wang, J. Chen, X. Ren, J. Zhang, J. Ding, Y. Liu, K.H. Lim, J. Wang, X. Li, H. Yang, Halogen-incorporated Sn catalysts for selective electrochemical CO_2 reduction to formate, Angew. Chem. Int. Ed. (2022), e202211174.

[22] H. Cheng, S. Liu, J. Zhang, T. Zhou, N. Zhang, X.-s Zheng, W. Chu, Z. Hu, C. Wu, Y. Xie, Surface nitrogen-injection engineering for high formation rate of CO_2 reduction to formate, Nano Lett. 20 (2020) 6097–6103.

[23] R.T. Hannagan, G. Giannakakis, M. Flytzani-Stephanopoulos, E.C.H. Sykes, Single-atom alloy catalysis, Chem. Rev. 120 (2020) 12044–12088.

[24] F. Chen, X. Jiang, L. Zhang, R. Lang, B. Qiao, Single-atom catalysis: Bridging the homo-and heterogeneous catalysis, Chin. J. Catal. 39 (2018) 893–898.

[25] X. Cui, W. Li, P. Ryabchuk, K. Junge, M. Beller, Bridging homogeneous and heterogeneous catalysis by heterogeneous single-metal-site catalysts, Nat. Catal. 1 (2018) 385–397.

[26] M.T. Greiner, T. Jones, S. Beeg, L. Zwiener, M. Scherzer, F. Girgsdies, S. Piccinin, M. Armbrüster, A. Knop-Gericke, R. Schlögl, Free-atom-like d states in single-atom alloy catalysts, Nat. Chem. 10 (2018) 1008–1015.

[27] X. Zhang, G. Cui, H. Feng, L. Chen, H. Wang, B. Wang, X. Zhang, L. Zheng, S. Hong, M. Wei, Platinum–copper single atom alloy catalysts with high performance towards glycerol hydrogenolysis, Nat. Commun. 10 (2019) 5812.

[28] J. Li, H. Zeng, X. Dong, Y. Ding, S. Hu, R. Zhang, Y. Dai, P. Cui, Z. Xiao, D. Zhao, L. Zhou, T. Zheng, J. Xiao, J. Zeng, C. Xia, Selective CO_2 electrolysis to CO using isolated antimony alloyed copper, Nat. Commun. 14 (2023) 340.

[29] H. Xie, Y. Wan, X. Wang, J. Liang, G. Lu, T. Wang, G. Chai, N.M. Adli, C. Priest, Y. Huang, Boosting Pd-catalysis for electrochemical CO_2 reduction to CO on Bi-Pd single atom alloy nanodendrites, Appl. Catal. B 289 (2021), 119783.

[30] G. Zhou, S. Zhao, T. Wang, S.-Z. Yang, B. Johannessen, H. Chen, C. Liu, Y. Ye, Y. Wu, Y. Peng, C. Liu, S.P. Jiang, Q. Zhang, Y. Cui, Theoretical calculation guided design of single-atom catalysts toward fast kinetic and long-life Li–S batteries, Nano Lett. 20 (2020) 1252–1261.

[31] Z. Han, S. Zhao, J. Xiao, X. Zhong, J. Sheng, W. Lv, Q. Zhang, G. Zhou, H.M. Cheng, Engineering d-p orbital hybridization in single-atom metal-embedded three-dimensional electrodes for Li–S batteries, Adv. Mater. 33 (2021), 2105947.

[32] X. Zhou, J. Shan, L. Chen, B.Y. Xia, T. Ling, J. Duan, Y. Jiao, Y. Zheng, S.-Z. Qiao, Stabilizing Cu2+ ions by solid solutions to promote CO_2 electroreduction to methane, J. Am. Chem. Soc. 144 (2022) 2079–2084.

[33] J. Hafner, Ab-initio simulations of materials using VASP: density-functional theory and beyond, J. Comput. Chem. 29 (2008) 2044–2078.

[34] M. Ernzerhof, G.E. Scuseria, Assessment of the perdew–burke–ernzerhof exchange-correlation functional, J. Chem. Phys. 110 (1999) 5029–5036.

[35] P. Wisesa, K.A. McGill, T. Mueller, Efficient generation of generalized Monkhorst-Pack grids through the use of informatics, Phys. Rev. B 93 (2016), 155109.

[36] J. Moellmann, S. Grimme, DFT-D3 study of some molecular crystals, J. Phys. Chem. C. 118 (2014) 7615–7621.

[37] J.K. Nørskov, J. Rossmeisl, A. Logadottir, L. Lindqvist, J.R. Kitchin, T. Bligaard, H. Jonsson, Origin of the overpotential for oxygen reduction at a fuel-cell cathode, J. Phys. Chem. B 108 (2004) 17886–17892.

[38] Y. Wang, Y. Gao, L. Sun, Y. Li, B. Zheng, W. Zhai, Effect of physical properties of Cu-Ni-graphite composites on tribological characteristics by grey correlation analysis, Results Phys. 7 (2017) 263–271.

[39] M.-S. Tsai, F.-Y. Hsu, Application of grey correlation analysis in evolutionary programming for distribution system feeder reconfiguration, IEEE Trans. Power Syst. 25 (2009) 1126–1133.

[40] Y.Y. Birdja, E. Pérez-Gallent, M.C. Figueiredo, A.J. Göttle, F. Calle-Vallejo, M.T. M. Koper, Advances and challenges in understanding the electrocatalytic conversion of carbon dioxide to fuels, Nat. Energy 4 (2019) 732–745.

[41] S. Hanselman, M.T. Koper, F. Calle-Vallejo, Computational comparison of late transition metal (100) surfaces for the electrocatalytic reduction of CO to C2 species, ACS Energy Lett. 3 (2018) 1062–1067.

[42] Y. Zhang, R. Yang, H. Li, Z. Zeng, Boosting electrocatalytic reduction of CO_2 to HCOOH on Ni single atom anchored WTe2 monolayer, Small 18 (2022), 2203759.

[43] A. Sharma, M. Varshney, H.J. Shin, B.-H. Lee, K.H. Chae, S.O. Won, Effect of Cu insertion on structural, local electronic/atomic structure and photocatalyst properties of TiO_2, ZnO and Ni (OH) 2 nanostructures: XANES-EXAFS study, Mater. Chem. Phys. 191 (2017) 129–144.

[44] L. Meng, E. Zhang, H. Peng, Y. Wang, D. Wang, H. Rong, J. Zhang, Bi/Zn dual single-atom catalysts for electroreduction of CO_2 to syngas, ChemCatChem 14 (2022), e202101801.

[45] C.B. Benda, T. Köchner, R. Schäper, S. Schulz, T.F. Fässler, Bi-Zn bond formation in liquid ammonia solution: [Bi- Zn-Bi] 4−, a Linear Polyanion that is Iso (valence)-electronic to CO_2, Angew. Chem. Int. Ed. 53 (2014) 8944–8948.

[46] L. Fan, C. Xia, P. Zhu, Y. Lu, H. Wang, Electrochemical CO_2 reduction to high-concentration pure formic acid solutions in an all-solid-state reactor, Nat. Commun. 11 (2020) 3633.

[47] M. Shao, R. Adzic, Electrooxidation of ethanol on a Pt electrode in acid solutions: in situ ATR-SEIRAS study, Electrochim. Acta 50 (2005) 2415–2422.

[48] J. Li, J. Li, X. Liu, J. Chen, P. Tian, S. Dai, M. Zhu, Y.-F. Han, Probing the role of surface hydroxyls for Bi, Sn and In catalysts during CO_2 Reduction, Appl. Catal. B 298 (2021), 120581.

[49] B. Innocent, D. Pasquier, F. Ropital, F. Hahn, J.-M. Léger, K. Kokoh, FTIR spectroscopy study of the reduction of carbon dioxide on lead electrode in aqueous medium, Appl. Catal. B 94 (2010) 219–224.

[50] M. Baruch, J. Pander, J. White, A. Bocarsly, Mechanistic insights into the reduction of CO_2 on tin electrodes using in situ ATR-IR spectroscopy, ACS Catal. 5 (2015) 3148–3156.

[51] C. Cao, D.D. Ma, J.F. Gu, X. Xie, G. Zeng, X. Li, S.G. Han, Q.L. Zhu, X.T. Wu, Q. Xu, Metal–organic layers leading to atomically thin bismuthene for efficient carbon dioxide electroreduction to liquid fuel, Angew. Chem. Int. Ed. 59 (2020) 15014–15020.

[52] T. Shen, S. Chen, C. Zhang, Y. Hu, E. Ma, Y. Yang, J. Hu, D. Wang, Engineering Ir atomic configuration for switching the pathway of formic acid electrooxidation reaction, Adv. Funct. Mater. 32 (2022), 2107672.

[53] K. Yao, J. Li, H. Wang, R. Lu, X. Yang, M. Luo, N. Wang, Z. Wang, C. Liu, T. Jing, Mechanistic insights into OC–COH coupling in CO_2 electroreduction on fragmented copper, J. Am. Chem. Soc. 144 (2022) 14005–14011.

[54] Y. Zhao, X. Zu, R. Chen, X. Li, Y. Jiang, Z. Wang, S. Wang, Y. Wu, Y. Sun, Y. Xie, Industrial-current-density CO_2-to-C2+ electroreduction by anti-swelling anion-exchange ionomer-modified oxide-derived Cu nanosheets, J. Am. Chem. Soc. 144 (2022) 10446–10454.

[55] Y. Li, C.-Z. Huo, H.-J. Wang, Z.-X. Ye, P.-P. Luo, X.-X. Cao, T.-B. Lu, Coupling CO_2 reduction with CH_3OH oxidation for efficient electrosynthesis of formate on hierarchical bifunctional CuSn alloy, Nano Energy 98 (2022), 107277.